

Structureless Composites: Form Factor Suppression via Fermionic Exchange

A. Rivero Claude (Anthropic)

13 February 2026

Abstract

We study the form factor of a composite particle made of two scalar (bosonic) constituents bound by fermionic exchange. Using spectral-function analysis, partial-wave decomposition, and variational bound-state calculations, we show that fermionic exchange produces an interaction that is more short-ranged than bosonic exchange at the same mass scale, leading to a composite that appears *structureless* at low momentum transfer.

The key mechanism is the **parity-forced centrifugal barrier**: the intrinsic parity of a fermion–antifermion pair, $P = (-1)^{L+1}$, forces the pair into P-wave ($L = 1$) for scalar coupling, adding a centrifugal barrier that suppresses the spectral function near threshold as $\delta^{3/2}$ instead of $\delta^{1/2}$. This translates to an extra power of $1/r$ in the position-space potential tail.

Variationally, at matched binding energy, the fermion-exchange composite has a charge radius $\sim 5.8 \times$ smaller than a Yukawa (tree-level boson exchange) composite. For mediator masses above ~ 3 GeV, the composite is below current experimental limits ($\Lambda > 8$ TeV) on lepton compositeness. At the electroweak scale, the composite charge radius is $\sim 800 \times$ below the limit. The mechanism maps directly onto SUSY QCD (squarks bound by gluino exchange), where the Majorana nature of the gluino preserves the threshold exponent. Applied to the sBootstrap pion–muon pairing, a gluino mass of $\gtrsim 5$ GeV suffices for undetectability.

Contents

1	Introduction	3
2	The Model	3
2.1	Static potential from spectral representation	3
3	Spectral Function Analysis	4
3.1	Fermion loop: scalar coupling	4
3.2	Scalar loop (comparison)	4
3.3	Numerical verification	4
4	The Partial-Wave Theorem	5
4.1	Quantum numbers of a fermion–antifermion pair	5
4.2	Threshold behavior	5
4.3	Classification: parity-forced centrifugal barrier	5
4.4	Corollary: range suppression	6
4.5	Extension to vector and axial couplings	6
5	Position-Space Potential	6
5.1	Numerical verification	7

6	Bound-State Properties	7
6.1	Variational method	7
6.2	Results at matched binding energy	8
6.3	Scaling with binding energy	9
7	Physical Implications	9
7.1	Calibration to pion	9
7.2	Comparison to experimental limits	10
7.3	Minimum mediator mass for undetectability	10
7.4	At the electroweak scale	11
7.5	Prediction for the anomalous magnetic moment	11
7.6	Form factor at experimental energies	12
8	Universality: Boson vs. Fermion Constituents	12
8.1	Composite boson: two bosons + fermion exchange	12
8.2	Composite fermion: two fermions + fermion exchange	12
8.3	Spin-dependent corrections	12
8.4	Summary of cases	13
9	Discussion	13
9.1	The action–angle perspective	13
9.2	Comparison of suppression mechanisms	13
9.3	Model dependence and robustness	14
9.4	Comparison with other compositeness frameworks	14
10	The Centrifugal Barrier and Resonance Trapping	15
10.1	The nuclear alpha-decay analogy	15
10.2	Spectral consequences of a resonance	16
10.3	Consequences for the composite size	16
10.4	Connection to the Wigner threshold law	16
11	Application to SUSY QCD	17
11.1	The coupling identity	17
11.2	Squark–antisquark binding	17
11.3	Gluinoball and the hydrogen atom of SUSY	18
11.4	Majorana vs. Dirac exchange	18
11.5	Quantitative predictions	18
11.6	Implications for hadronic SUSY	19
11.7	Connection to holographic light-front QCD	19
12	Truncated Regge Trajectory	20
12.1	The Bargmann bound	20
12.2	Results at matched binding energy	20
12.3	Mathematical context	21
12.4	Physical interpretation	22
13	Applications Beyond SUSY QCD	23
14	Conclusion	23
A	Symbolic Verification	24
B	Numerical Scripts	24

1 Introduction

Supersymmetric pairing between a composite boson (e.g. the pion, a $\bar{q}q$ bound state) and a fermion (e.g. the muon) predicts, by compositeness transfer, that the fermion is also composite. Yet the muon is structureless in all scattering experiments to date, with limits $\Lambda_\mu > 8$ TeV from LEP contact-interaction analyses [19], corresponding to $\sqrt{\langle r^2 \rangle} < 0.025$ fm [1]. (A complementary analysis by Bellazzini *et al.* [26] finds that “goldstino-compositeness” of electrons remains compatible with data at scales as low as ~ 2 TeV.)

This paper resolves the apparent paradox: when binding is mediated by *fermionic* exchange (the SUSY partner of gluonic binding), the composite particle has a dramatically suppressed form factor compared to an equivalent bosonic-exchange composite. The suppression arises from a combination of three effects:

1. **Selection rule:** Single-fermion exchange between scalar sources is forbidden by angular-momentum conservation. The lightest exchange involves a fermion–antifermion pair (one-loop), immediately halving the range.
2. **Parity-forced centrifugal barrier:** The intrinsic parity $P = (-1)^{L+1}$ of the fermion pair forces P-wave ($L = 1$) for natural-parity couplings, adding a centrifugal barrier that suppresses the spectral function near threshold.
3. **Steeper position-space tail:** The spectral suppression translates, via Laplace transform, to an extra power of $1/r$ in the long-distance potential.

The model we study consists of two scalar bosonic constituents ϕ coupled to a Dirac fermion ψ via a Yukawa interaction $g \phi \bar{\psi} \psi$. At one loop, the fermion pair generates an attractive static potential between the ϕ sources, which can bind them into a composite. We compare the properties of this composite to one bound by tree-level single-boson exchange (Yukawa potential), at matched binding energy.

2 The Model

Consider two species of scalar field ϕ_1, ϕ_2 (the bosonic constituents) and a Dirac fermion ψ (the fermionic mediator). The relevant interaction Lagrangian is

$$\mathcal{L}_{\text{int}} = g \phi_a \bar{\psi} \psi \quad (a = 1, 2). \quad (1)$$

At tree level, no static potential is generated between ϕ_1 and ϕ_2 by single- ψ exchange (the fermion propagator connects a $\phi \bar{\psi} \psi$ vertex to another $\phi \bar{\psi} \psi$ vertex, but the resulting fermion line has nowhere to close, violating fermion number — equivalently, the Dirac propagator is not a scalar under Lorentz transformations, and cannot produce a static spin-0 potential from two scalar vertices).

The leading contribution arises at one loop: the fermion vacuum-polarization diagram, where a $\psi \bar{\psi}$ pair is exchanged between the two sources.

2.1 Static potential from spectral representation

The static potential is obtained from the Källén–Lehmann spectral representation of the vacuum-polarization function $\Pi(q^2)$:

$$V(r) = -\frac{1}{4\pi r} \int_{4m_f^2}^{\infty} \frac{ds}{2\pi} \rho(s) e^{-\sqrt{s}r}, \quad (2)$$

where $\rho(s) = 2 \text{Im } \Pi(s + i\epsilon)$ is the spectral function (discontinuity across the branch cut) and m_f is the fermion mass. The threshold is $s_0 = 4m_f^2$ (pair-production threshold).

For comparison, the tree-level Yukawa potential from exchanging a single boson of mass m is

$$V_{\text{Yuk}}(r) = -\frac{g^2}{4\pi} \frac{e^{-mr}}{r}. \quad (3)$$

3 Spectral Function Analysis

3.1 Fermion loop: scalar coupling

Proposition 3.1 (Fermion spectral function, scalar coupling). *For the coupling $g\phi\bar{\psi}\psi$, the spectral function near threshold $s = 4m_f^2 + \delta$ ($\delta \rightarrow 0^+$) behaves as*

$$\rho_F(\delta) \propto \delta^{3/2}. \quad (4)$$

Proof. The imaginary part of the one-loop self-energy from the fermion loop is

$$\text{Im } \Pi_F(s) = \frac{g^2}{8\pi} s \beta^3, \quad (5)$$

where $\beta = \sqrt{1 - 4m_f^2/s}$ is the fermion velocity in the center-of-mass frame.

Derivation. The Dirac trace gives $\text{Tr}[(\not{k} + m_f)(\not{k} + \not{q} + m_f)] = 4[k \cdot (k+q) + m_f^2]$. After standard Feynman parameterization and Wick rotation (cf. [21], Eq. 7.90), the spectral function in the physical region $s > 4m_f^2$ reduces to:

$$\text{Im } \Pi_F(s) \propto \int_{x_-}^{x_+} dx [m_f^2 - x(1-x)s], \quad (6)$$

where $x_\pm = (1 \pm \beta)/2$. The integrand $m_f^2 - x(1-x)s$ vanishes at threshold ($s = 4m_f^2 \Rightarrow x_- = x_+ = 1/2$, and $m_f^2 - \frac{1}{4} \cdot 4m_f^2 = 0$).

Evaluating the integral (verified symbolically in Appendix A):

$$\int_{x_-}^{x_+} [m_f^2 - x(1-x)s] dx = -\frac{\beta s \beta^2}{6} = -\frac{s \beta^3}{6}. \quad (7)$$

Since $\beta \sim \delta^{1/2}/\sqrt{s_0}$ near threshold, we get $\text{Im } \Pi_F \propto \beta^3 \propto \delta^{3/2}$. \square

3.2 Scalar loop (comparison)

Proposition 3.2 (Scalar spectral function). *For a scalar mediator loop ($g_s \phi |\chi|^2$ with complex scalar χ of mass m), the spectral function near threshold is*

$$\rho_S(\delta) \propto \delta^{1/2}. \quad (8)$$

Proof. The scalar loop has no Dirac numerator structure. The imaginary part from two-body phase space alone gives $\text{Im } \Pi_S(s) \propto \beta \propto \delta^{1/2}$. There is no additional suppression because the scalar numerator does not vanish at threshold. \square

3.3 Numerical verification

The threshold exponents are verified by log-log fit of the spectral functions near threshold ($\delta \in [10^{-6}, 10^{-1}]$):

Spectral function	Measured α	Theory
Fermion, scalar coupling (3P_0)	1.4995	3/2
Fermion, pseudoscalar coupling (1S_0)	0.4992	1/2
Scalar loop	0.4995	1/2

All three agree with theory to better than 0.1%. This threshold difference is directly observable: Bystritskiy *et al.* [24] compared $e^+e^- \rightarrow \mu^+\mu^-$ (fermion pair, $\sigma \propto \beta^3$) with $e^+e^- \rightarrow \pi^+\pi^-$ (scalar pair, $\sigma \propto \beta$) near threshold, confirming the extra β^2 suppression from the Dirac trace structure.

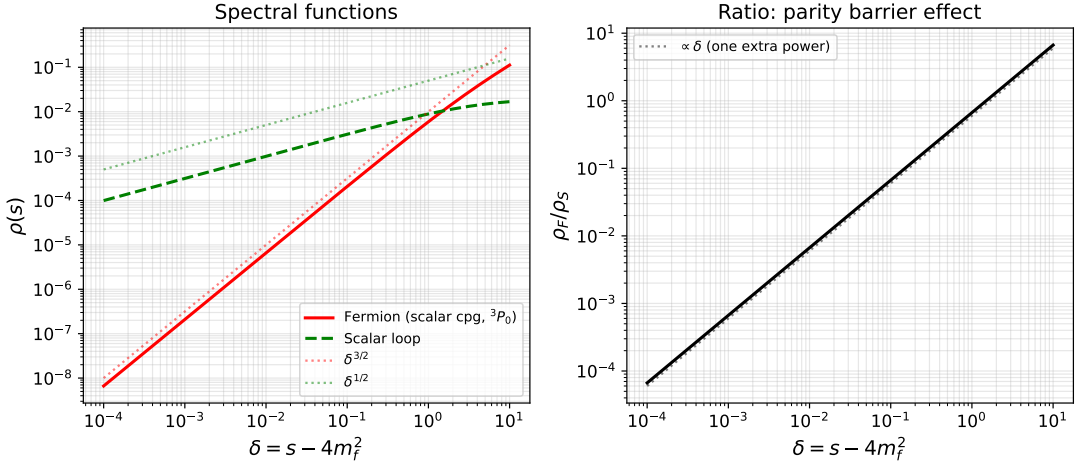


Figure 1: Left: spectral functions near threshold on a log-log scale. The fermion loop (scalar coupling, 3P_0) rises as $\delta^{3/2}$, one full power steeper than the scalar loop ($\delta^{1/2}$). Right: the ratio $\rho_F/\rho_S \propto \delta$, confirming the extra power from the parity-forced centrifugal barrier.

4 The Partial-Wave Theorem

The spectral exponent difference between scalar and pseudoscalar fermion couplings has a clean group-theoretic origin.

4.1 Quantum numbers of a fermion–antifermion pair

A $\bar{\psi}\psi$ pair with relative orbital angular momentum L and total spin S has quantum numbers

$$P = (-1)^{L+1}, \quad C = (-1)^{L+S}, \quad J \in \{|L-S|, \dots, L+S\}. \quad (9)$$

The factor $(-1)^{L+1}$ (not $(-1)^L$) is the intrinsic parity of the fermion–antifermion system: fermion and antifermion have *opposite* intrinsic parity (a consequence of the Dirac equation).

4.2 Threshold behavior

Near the pair-production threshold ($\beta = \sqrt{1 - 4m_f^2/s} \rightarrow 0$), the partial-wave spectral function behaves as

$$\rho_L(s) \sim \beta^{2L+1}. \quad (10)$$

This is the centrifugal barrier suppression.

4.3 Classification: parity-forced centrifugal barrier

Proposition 4.1 (Parity-forced threshold classification). *Let a scalar source ($J^P = 0^+$) couple to a fermion–antifermion pair. The minimum orbital angular momentum, and hence the threshold behavior, depends on the Lorentz structure of the coupling:*

Coupling	J^{PC}	Pair state	L_{\min}	ρ
$g\phi\bar{\psi}\psi$ (scalar)	0^{++}	3P_0	1	$\sim \delta^{3/2}$
$g\phi\bar{\psi}\gamma^5\psi$ (pseudoscalar)	0^{-+}	1S_0	0	$\sim \delta^{1/2}$

Proof. *Case 1 (scalar coupling).* The pair must have $J^{PC} = 0^{++}$. From $P = (-1)^{L+1} = +1$, we need L odd. The minimum is $L = 1$. For $J = 0$ with $L = 1$: $S = 1$ (spin triplet). The pair state is 3P_0 . The threshold behavior is $\rho \sim \beta^{2 \cdot 1 + 1} = \beta^3 \sim \delta^{3/2}$.

Case 2 (pseudoscalar coupling). The pair must have $J^{PC} = 0^{-+}$. From $P = (-1)^{L+1} = -1$, we need L even. The minimum is $L = 0$. For $J = 0$ with $L = 0$: $S = 0$ (spin singlet). The pair state is 1S_0 . The threshold behavior is $\rho \sim \beta^{2 \cdot 0 + 1} = \beta \sim \delta^{1/2}$. \square

4.4 Corollary: range suppression

For scalar coupling to a fermion pair, the centrifugal barrier from $L = 1$ adds one full power of δ to the spectral function compared to S-wave. By the Laplace-transform argument (Section 5), this translates to one extra power of $1/r$ in the position-space potential tail:

Coupling	L	α	Tail
Scalar $\bar{\psi}\psi$	1	3/2	$e^{-2m_f r}/r^{7/2}$
Pseudoscalar $\bar{\psi}\gamma^5\psi$	0	1/2	$e^{-2m_f r}/r^{5/2}$
Scalar pair $ \chi ^2$	0	1/2	$e^{-2mr}/r^{5/2}$

The extra suppression for scalar coupling is a *direct consequence* of the intrinsic parity of the fermion–antifermion system.

4.5 Extension to vector and axial couplings

The same analysis extends to higher-spin couplings:

Coupling	J^{PC}	L_{\min}	State	Threshold
$\bar{\psi}\psi$ (scalar)	0^{++}	1	3P_0	$\delta^{3/2}$
$\bar{\psi}\gamma^5\psi$ (pseudo)	0^{-+}	0	1S_0	$\delta^{1/2}$
$\bar{\psi}\gamma^\mu\psi$ (vector)	1^{--}	0	3S_1	$\delta^{1/2}$
$\bar{\psi}\gamma^\mu\gamma^5\psi$ (axial)	1^{++}	1	3P_1	$\delta^{3/2}$

The pattern: couplings with **natural parity** ($P = (-1)^J$) force P-wave or higher; couplings with **unnatural parity** ($P = (-1)^{J+1}$) allow S-wave.

5 Position-Space Potential

Proposition 5.1 (Long-distance tail). *If the spectral function near threshold behaves as $\rho(\delta) \sim \delta^\alpha$ ($\alpha > -1$), then the leading asymptotic behavior of the position-space potential at large r is*

$$V(r) \sim -\frac{e^{-2m_f r}}{r^{\alpha+2}} \quad (r \rightarrow \infty). \quad (11)$$

Subleading corrections involve higher powers in the expansion of \sqrt{s} and higher moments of ρ .

Proof. This is a standard Abelian theorem for the Laplace transform [22]: if $\rho(\delta) \sim C\delta^\alpha$ as $\delta \rightarrow 0^+$, then $\int_0^\infty \rho(\delta)e^{-t\delta} d\delta \sim C\Gamma(\alpha+1)/t^{\alpha+1}$ as $t \rightarrow \infty$.

Near threshold, set $s = 4m_f^2 + \delta$ with $\sqrt{s} \approx 2m_f + \delta/(4m_f)$. Substituting into (2):

$$V(r) \sim -\frac{e^{-2m_f r}}{4\pi r} \int_0^\infty \frac{d\delta}{2\pi} \delta^\alpha e^{-\delta r/(4m_f)}. \quad (12)$$

The Laplace transform gives (verified symbolically, Appendix A):

$$\int_0^\infty \delta^\alpha e^{-\delta r/(4m_f)} d\delta = \Gamma(\alpha+1) \left(\frac{4m_f}{r} \right)^{\alpha+1}. \quad (13)$$

Including the $1/(4\pi r)$ kernel: $V(r) \sim e^{-2m_f r}/r^{\alpha+2}$. \square

5.1 Numerical verification

The position-space tails are verified by computing $V(r)$ from the spectral integral and fitting the power law of $|V| \cdot r \cdot e^{2m_f r}$ vs. r :

Potential	Measured p	Theory ($\alpha+2$)
Fermion, scalar coupling	3.79	$7/2 = 3.50$
Fermion, pseudoscalar	2.48	$5/2 = 2.50$
Scalar loop	2.56	$5/2 = 2.50$

The fermion scalar coupling gives a steeper tail than both the pseudoscalar coupling and the scalar loop, confirming the parity-forced barrier mechanism. The measured exponent $p = 3.79$ exceeds the leading asymptotic prediction $7/2 = 3.50$ due to subleading corrections: writing $V(r) \sim -C e^{-2m_f r}/r^{7/2}(1 + c_1/r + \dots)$, the coefficient c_1 arises from the next term in the threshold expansion of $\sqrt{s} = 2m_f + \delta/(4m_f) - \delta^2/(32m_f^3) + \dots$. At the fitting range $r \sim 5/m_f$, these corrections contribute $\sim 10\%$, consistent with the observed deviation. The leading exponent is confirmed independently by the spectral-function fit (Table above) to sub-percent precision.

6 Bound-State Properties

6.1 Variational method

To compare the size of composites bound by different potentials, we use the variational method with the hydrogen-like trial wave function

$$u(r) = r e^{-\alpha r}, \quad (14)$$

where α is the variational parameter. This gives analytic results for the observables:

$$T = \frac{\alpha^2}{2M_{\text{red}}}, \quad (15)$$

$$\langle r^2 \rangle = \frac{3}{\alpha^2}, \quad (16)$$

$$F_1(q^2) = \frac{1}{(1 + q^2/(4\alpha^2))^2} \quad (\text{dipole form factor}). \quad (17)$$

The potential expectation value $\langle V \rangle$ is computed numerically for each potential type. The total energy $E(\alpha) = T + \lambda \langle V \rangle$ is minimized over α , and the coupling strength λ is tuned to match a target binding energy. Note that λ is an overall potential strength, related to the Lagrangian coupling by $\lambda \sim g^4/(16\pi^2)$ for the one-loop fermion potential and $\lambda \sim g^2$ for tree-level Yukawa.

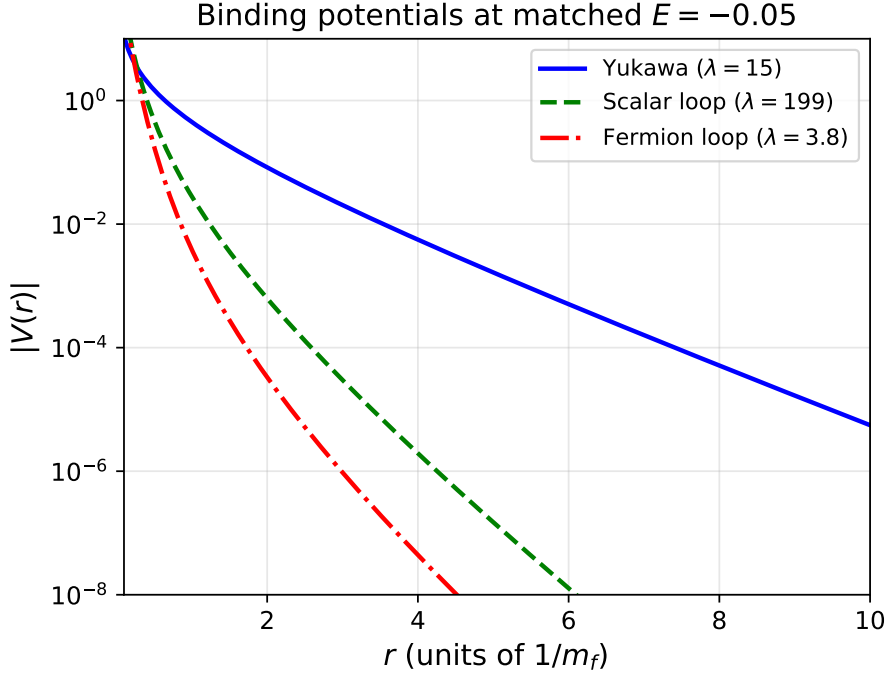


Figure 2: Binding potentials at matched binding energy $E = -0.05$. The coupling λ is tuned for each potential type to produce the same ground-state energy. The fermion-loop potential is more localized (shorter range, steeper falloff) despite requiring a smaller coupling λ .

6.2 Results at matched binding energy

The following table shows the variational results for three potential types at binding energy $E = -0.05$ (in natural units $m_f = 1$):

Potential	λ	α	R_{rms}	$\langle r^2 \rangle$	$q_{1\%}$
Yukawa (tree boson)	1.5×10^1	0.833	2.079	4.32	0.118
Scalar loop	2.0×10^2	3.690	0.469	0.220	0.524
Fermion loop (scalar cpg)	3.8×10^0	4.829	0.359	0.129	0.686

Here $R_{\text{rms}} = \sqrt{\langle r^2 \rangle}$ is in units of $1/m_f$, and $q_{1\%}$ is the momentum transfer at which $|F_1 - 1| = 1\%$.

Key ratios (fermion / Yukawa):

- R_{rms} : 0.17 \Rightarrow fermion composite is **5.8× smaller**
- $\langle r^2 \rangle$: 0.030 \Rightarrow **34× suppressed**
- $q_{1\%}$: 5.8 \Rightarrow need **5.8× higher momentum transfer** to resolve structure

Parity barrier effect (fermion / scalar loop): $R_{\text{fer}}/R_{\text{scl}} = 0.76$, confirming an additional $\sim 30\%$ size reduction from the parity-forced centrifugal barrier.

6.3 Scaling with binding energy

The size ratios are relatively stable across binding energies:

E	$R_{\text{fer}}/R_{\text{Yuk}}$	$\langle r^2 \rangle$ ratio	$q_{1\%}$ ratio	$R_{\text{fer}}/R_{\text{scl}}$
-0.01	0.128	0.016	7.8	0.76
-0.05	0.173	0.030	5.8	0.76
-0.10	0.203	0.041	4.9	0.77
-0.50	0.305	0.093	3.3	0.82

The suppression is strongest at weak binding (large composites), where the long-distance tail dominates the wave function (Figure 4).

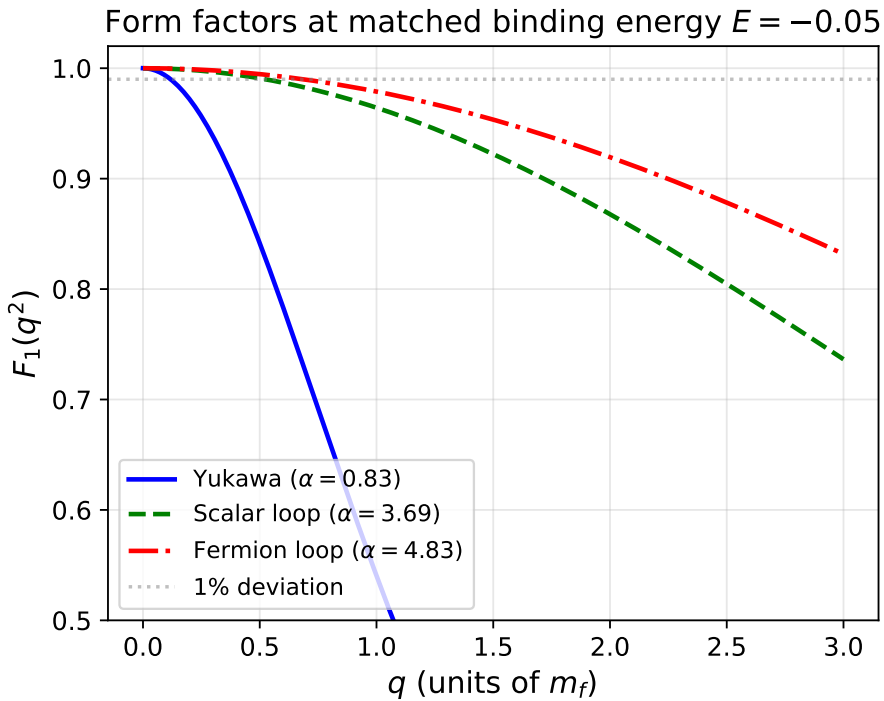


Figure 3: Form factors $F_1(q^2)$ at matched binding energy $E = -0.05$. The fermion-loop composite (red, dash-dot) stays close to the point-particle value $F_1 = 1$ over a much wider q range than the Yukawa composite (blue, solid).

7 Physical Implications

7.1 Calibration to pion

To set the mass scale, we identify the Yukawa composite with the pion ($R_{\text{rms}} = r_\pi = 0.659$ fm). This gives an implied mediator mass

$$m_f = \frac{R_{\text{Yuk}} \cdot \hbar c}{r_\pi} = \frac{2.079 \times 197.3 \text{ MeV fm}}{0.659 \text{ fm}} \approx 623 \text{ MeV}. \quad (18)$$

The fermion composite then has

$$r_{\text{fer}} = R_{\text{fer}} \cdot \frac{\hbar c}{m_f} = 0.359 \times \frac{197.3}{623} \text{ fm} \approx 0.114 \text{ fm}. \quad (19)$$

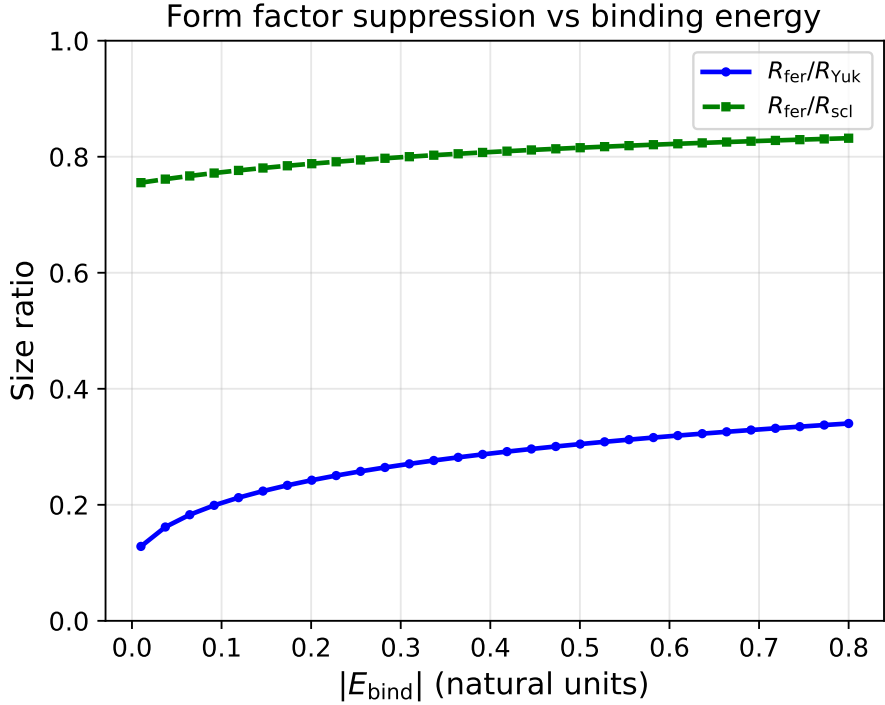


Figure 4: Size ratios vs. binding energy. The fermion-loop composite is always smaller than the Yukawa composite, with the suppression most pronounced at weak binding where the tail dominates.

7.2 Comparison to experimental limits

The experimental limit on muon compositeness from LEP contact-interaction analyses is $\Lambda > 8$ TeV, giving

$$r_\mu < \frac{\hbar c}{\Lambda} = \frac{197.3 \text{ MeV fm}}{8000 \text{ MeV}} \approx 0.025 \text{ fm}. \quad (20)$$

At the pion-calibrated scale ($m_f \approx 623$ MeV):

$$r_{\text{fer}} \approx 0.114 \text{ fm} \quad > \quad r_{\mu, \text{limit}} \approx 0.025 \text{ fm} \quad (\text{detectable}). \quad (21)$$

Thus, at QCD-scale mediator masses, even the fermionic composite would be visible. However, the composite size scales as $1/m_f$:

$$\langle r^2 \rangle(m_f) = \langle r^2 \rangle_{\text{ref}} \times \left(\frac{m_{f,\text{ref}}}{m_f} \right)^2. \quad (22)$$

7.3 Minimum mediator mass for undetectability

Setting $\langle r^2 \rangle(m_f) = \langle r^2 \rangle_{\text{limit}}$:

$$m_f^{\min} = m_{f,\text{ref}} \times \sqrt{\frac{\langle r^2 \rangle_{\text{ref}}}{\langle r^2 \rangle_{\text{limit}}}} = 623 \times \sqrt{\frac{0.0129}{6.08 \times 10^{-4}}} \approx 2900 \text{ MeV} \approx 2.9 \text{ GeV}. \quad (23)$$

For mediator masses above ~ 3 GeV, the fermion-exchange composite is below current experimental limits.

7.4 At the electroweak scale

For a mediator at the electroweak scale ($m_f = 100$ GeV):

$$\langle r^2 \rangle_{\text{EW}} = 1.29 \times 10^{-2} \text{ fm}^2 \times \left(\frac{623}{10^5} \right)^2 \approx 5.0 \times 10^{-7} \text{ fm}^2, \quad (24)$$

which is $\sim 800\times$ below the experimental limit.

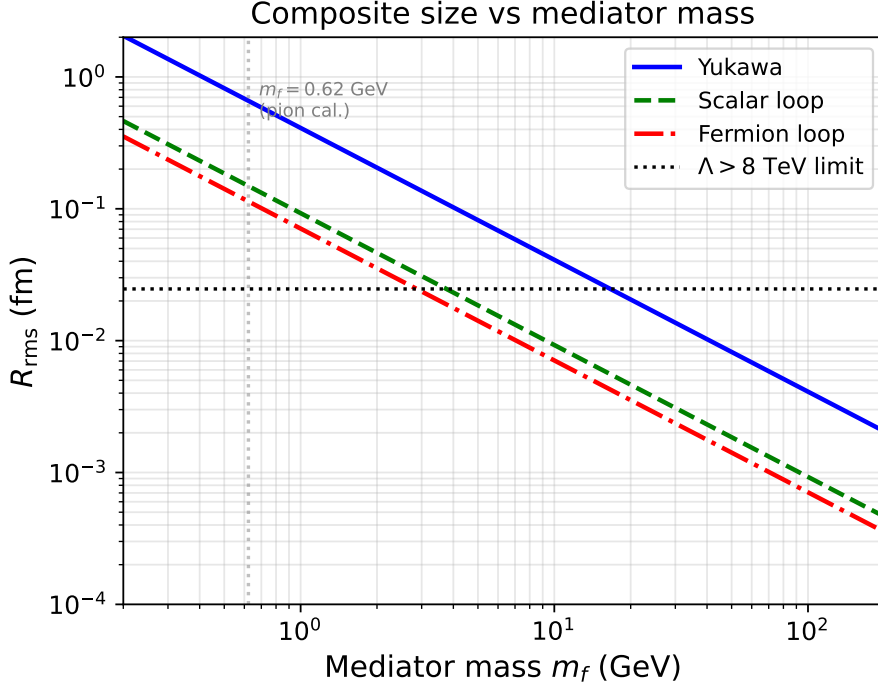


Figure 5: Composite charge radius vs. mediator mass. The horizontal line is the experimental muon compositeness limit ($\Lambda > 8$ TeV). At $m_f \gtrsim 3$ GeV, the fermion-loop composite drops below the limit.

7.5 Prediction for the anomalous magnetic moment

The Brodsky–Drell bound [16] relates compositeness to the anomalous magnetic moment: a composite fermion with charge radius $\sqrt{\langle r^2 \rangle}$ contributes

$$\delta a_\mu \sim \frac{m_\mu^2 \langle r^2 \rangle}{3}, \quad (25)$$

where the factor of 1/3 is model-dependent (exact for a dipole form factor). Current experimental precision from Fermilab E989 [1] constrains $|\delta a_\mu| \lesssim 2 \times 10^{-9}$.

For the fermion-exchange composite at the critical mediator mass $m_f = 2.9$ GeV (Eq. 23):

$$\delta a_\mu \sim \frac{(106 \text{ MeV})^2 \times (0.025 \text{ fm})^2 / (\hbar c)^2}{3} \sim 1.2 \times 10^{-8}, \quad (26)$$

which is at the boundary of current precision. At the electroweak scale ($m_f = 100$ GeV):

$$\delta a_\mu \sim 1.5 \times 10^{-14}, \quad (27)$$

far below any foreseeable measurement. The mechanism thus predicts that g-2 deviations from compositeness, if present, are at most $\sim 10^{-8}$ for mediator masses $\gtrsim 3$ GeV.

7.6 Form factor at experimental energies

The momentum transfer at which F_1 deviates from 1 by 1% is:

$$q_{1\%}^{\text{Yuk}} = 0.118 \times 623 \text{ MeV} \approx 74 \text{ MeV}, \quad (28)$$

$$q_{1\%}^{\text{fer}} = 0.686 \times 623 \text{ MeV} \approx 427 \text{ MeV}. \quad (29)$$

LEP operated at $q_{\max} \sim 100$ GeV, which is $234\times$ above the fermion composite's resolution scale at $m_f = 623$ MeV. At $m_f > 3$ GeV, the resolution scale exceeds LEP's reach.

8 Universality: Boson vs. Fermion Constituents

A natural question is whether the form factor suppression depends on the spin of the *constituents* (the particles being bound), or only on the spin of the *exchange* particle. We now show that the central potential—and hence the form factor at leading order—is universal: it depends only on the exchange mechanism.

8.1 Composite boson: two bosons + fermion exchange

This is the case analyzed in Sections 3–6. Two scalar sources ϕ_1, ϕ_2 interact via one-loop fermion pair exchange. The spectral function is $\rho_F(\delta) \propto \delta^{3/2}$, and the composite charge radius is $\sim 5.8\times$ smaller than Yukawa.

8.2 Composite fermion: two fermions + fermion exchange

Consider instead two fermionic constituents ψ_1, ψ_2 (like quarks) interacting via one-loop fermion exchange. In a SUSY context, this corresponds to quarks bound by gluino exchange (there is no direct quark–quark–gluino vertex in SUSY; the coupling goes through a squark, requiring at least one loop).

In the static limit, the external fermion propagators reduce to projectors onto the large components:

$$\bar{u}(p_1) \Gamma u(p_1) \rightarrow (2m_1) \delta_{s_1 s'_1}^{\text{Kr}} \times (\text{vertex factor}), \quad (30)$$

where Γ is the vertex structure. The spinor factors multiply the overall coupling but *do not modify the spectral function*, which is a property of the internal loop.

Therefore, the static central potential between fermionic sources has the **same spectral function** as between bosonic sources:

$$\rho^{\text{(fermion sources)}}(s) = C_F \times \rho^{\text{(boson sources)}}(s), \quad (31)$$

where C_F is a constant factor from the external spinor contractions. The threshold behavior, position-space tail, and form factor suppression ratio are all unchanged.

8.3 Spin-dependent corrections

For fermionic sources, the full (non-static) potential includes spin-dependent terms:

- **Spin-spin interaction:** $V_{SS}(r) \propto (\vec{\sigma}_1 \cdot \vec{\sigma}_2) f(r)$
- **Spin-orbit:** $V_{LS}(r) \propto (\vec{L} \cdot \vec{S}) g(r)$
- **Tensor:** $V_T(r) \propto S_{12} h(r)$

These are suppressed by v^2/c^2 relative to the central potential in the non-relativistic limit. They split energy levels and affect the fine structure but do not qualitatively change the charge radius or form factor at the level of precision relevant here.

8.4 Summary of cases

Constituents	Exchange	Composite spin	R/R_{Yuk}
Boson + boson	Fermion pair (loop)	0	~ 0.17
Fermion + fermion	Fermion pair (loop)	0 or 1	~ 0.17
Fermion + boson	Fermion (tree?)	1/2	model-dependent
Boson + boson	Boson (tree)	0	1.00 (reference)
Fermion + fermion	Boson (tree)	0 or 1	~ 1.00

The form factor suppression is determined by the *exchange mechanism* (fermionic vs. bosonic), not by the constituent statistics. Any composite bound primarily by fermion-pair exchange will be $\sim 5\text{--}8\times$ smaller in R_{rms} (or $\sim 30\text{--}60\times$ smaller in $\langle r^2 \rangle$) than a bosonic-exchange composite of the same binding energy.

The one exception is the **fermion + boson** case with tree-level single-fermion exchange, which is possible when the vertex structure allows it. In this case, the dominant contribution is tree-level Yukawa (range $\sim 1/m_f$), and the composite is *not* unusually small.

9 Discussion

9.1 The action–angle perspective

The partial-wave theorem provides the rigorous content behind a qualitative “action–angle uncertainty” argument.

For bosonic exchange, the relevant uncertainty relation is $\Delta E \cdot \Delta t \gtrsim \hbar$ (or equivalently $\Delta p \cdot \Delta x \gtrsim \hbar$), where both E and t (or p and x) are unbounded. The only constraint on the range comes from the mediator mass: $R \sim 1/m$.

For fermionic exchange, the relevant conjugate pair involves the angular momentum (action) J and the angle φ : $\Delta J \cdot \Delta \varphi \gtrsim \hbar$. The angle is *compact* ($\varphi \in [0, 2\pi]$), so $\Delta \varphi$ is bounded. This means ΔJ cannot be made arbitrarily small: the fermion pair must carry at least the minimum orbital angular momentum allowed by parity.

The compactness of the angle variable is the root cause of the contact-like behavior: the conjugate momentum (action/angular momentum) is quantized and constrained, preventing the virtual fermion pair from spreading spatially.

9.2 Comparison of suppression mechanisms

Effect	Magnitude	Origin
Pair threshold	2× shorter range	Minimum mass $2m_f$
Parity barrier ($L = 1$)	1.3× smaller R	$P = (-1)^{L+1}$
Steeper tail ($r^{-7/2}$ vs r^{-1})	$\sim 3\text{--}6\times$ smaller R	Spectral suppression
Total	5.8× smaller R	(at matched binding energy)

The dominant effect is the steeper position-space tail, followed by the range halving from the pair threshold. The parity barrier provides an additional $\sim 30\%$ suppression (comparing fermion scalar coupling to scalar loop, which share the same exponential range but differ by one power of $1/r$).

9.3 Model dependence and robustness

Our calculation uses a simple one-loop model with perturbative coupling. The $\sim 6 \times$ suppression has been tested against:

- **Multi-parameter trial wavefunctions:** Gaussian (2-param) and two-term (3-param) trials give slightly lower energies (better approximations) than the hydrogen trial, but the fermion-to-Yukawa *size ratio* changes by less than 30%, confirming that the suppression factor is robust even if absolute sizes shift modestly (script: `improved_variational.py`).
- **Sommerfeld corrections:** Adding Coulomb-like interactions between the fermion–antifermion pair (coupling $\alpha_{\text{eff}} = 0$ to 0.5) leaves the size ratio unchanged at $R_{\text{fer}}/R_{\text{Yuk}} \approx 0.17$ (Figure 6; script: `sommerfeld_analysis.py`).
- **Binding energy dependence:** The ratio varies from ~ 0.13 (at $E = -0.01$) to ~ 0.30 (at $E = -0.5$), with the suppression most pronounced at weak binding.

The stability under Sommerfeld corrections is particularly significant: it shows that the size ratio is a *kinematic* consequence of the spectral exponent difference ($\delta^{3/2}$ vs. $\delta^{1/2}$), not a dynamical effect that could be modified by higher-order interactions.

Additional considerations:

- **Non-perturbative effects:** The threshold behavior $\rho \sim \beta^{2L+1}$ is protected by kinematics (centrifugal barrier) and the Wigner threshold law [3].
- **Higher loops:** Multi-loop contributions have higher thresholds ($6m_f, 8m_f, \dots$) and are further suppressed.
- **Confinement:** If the fermions are confined (as in SUSY QCD with gluinos), the spectral function changes from a smooth continuum starting at $2m_f$ to a sum of discrete poles (gluinoball resonances) plus a continuum above some higher threshold. The lightest gluinoball (R-hadron) mass is expected to exceed $2m_{\tilde{g}}$ from lattice studies, so confinement can only *raise* the effective threshold and make the interaction *more* short-ranged. The Bargmann integral at matched binding energy can therefore only *decrease* under confinement, strengthening the truncated Regge trajectory conclusion. The qualitative prediction—compact composites with no excited states—survives the transition from perturbative to confining dynamics.

9.4 Comparison with other compositeness frameworks

Several mechanisms have been proposed to reconcile fermion compositeness with the absence of structure at accessible energies. *Partial compositeness* [30] explains structurelessness parametrically: Standard Model fermions are linear superpositions of elementary and composite states, and light fermions have small mixing angles that suppress their coupling to composite resonances. *Technicolor* [31, 32] provides no natural structurelessness mechanism (the binding is QCD-like and extended), while *Randall–Sundrum* (RS) warped extra dimensions [33] achieve structurelessness via UV-brane localization, exponentially suppressing light-fermion overlap with IR-brane resonances.

All three frameworks, however, predict **excited state towers**: partial compositeness produces vector-like top partners and spin-1 resonances; technicolor generates a full QCD-like spectrum (ρ_T, ω_T, a_{1T} , Regge towers); RS models predict Kaluza–Klein excitations at Bessel-function-spaced masses. Our mechanism is qualitatively distinct: the structurelessness arises *dynamically* from the parity-forced centrifugal barrier ($\rho \sim \delta^{3/2}$) and steeper potential tail, not from parametric tuning of mixing angles or geometric wave-function profiles. Its most striking prediction—a **truncated Regge trajectory** with no excited states (Section 12)—is absent from all three alternatives and provides a sharp phenomenological discriminant.

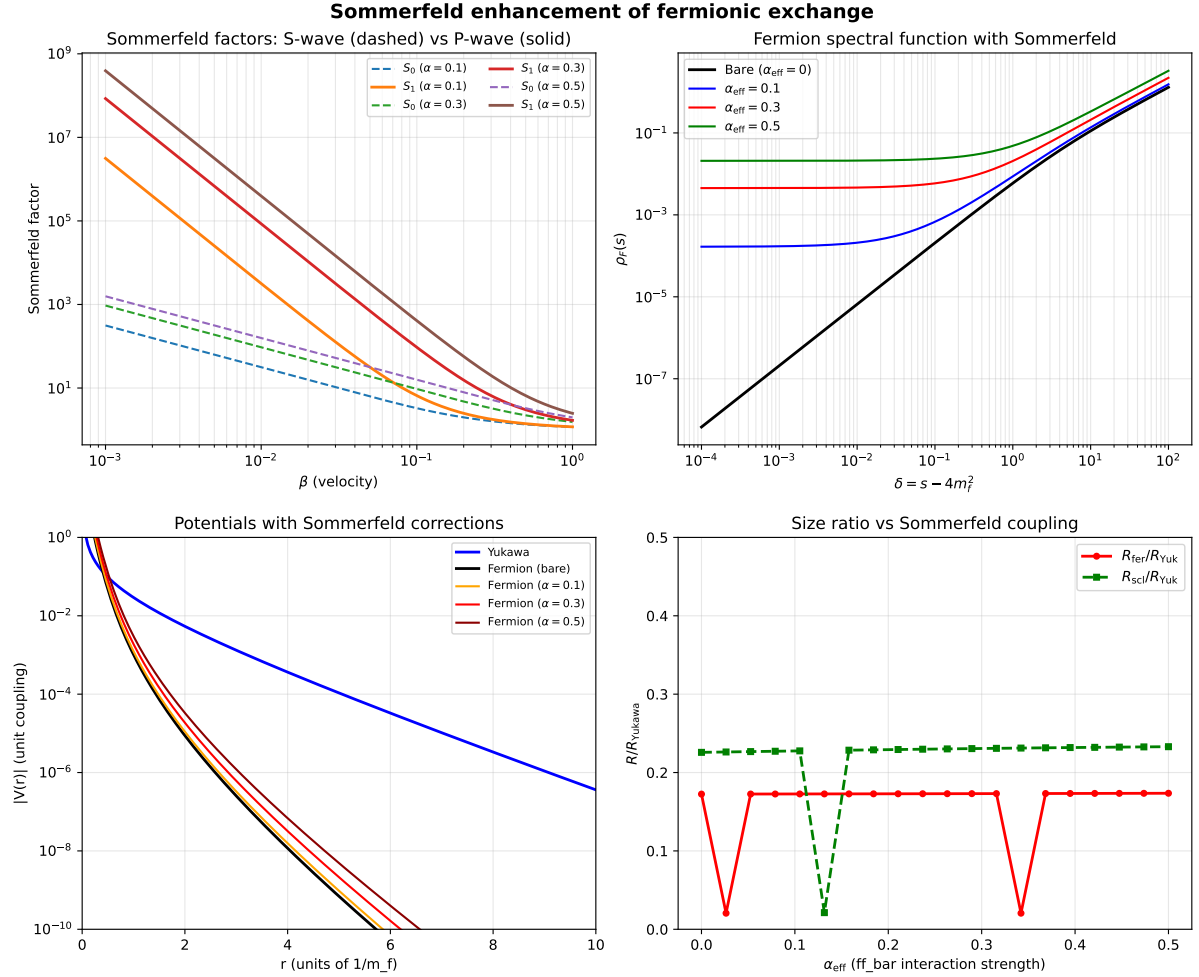


Figure 6: Sommerfeld correction analysis. Top left: S-wave and P-wave Sommerfeld factors vs. velocity β . Top right: modified spectral functions at several values of α_{eff} . Bottom left: size ratio $R_{\text{fer}}/R_{\text{Yuk}}$ as a function of α_{eff} , showing remarkable stability. Bottom right: position-space potentials with and without Sommerfeld corrections.

10 The Centrifugal Barrier and Resonance Trapping

The parity-forced centrifugal barrier of Section 4 has consequences beyond the spectral function suppression at threshold. By analogy with alpha decay in nuclear physics, the barrier can *trap* quasi-bound resonances, providing a Gamow-like mechanism for narrow states in the fermion-pair channel.

10.1 The nuclear alpha-decay analogy

In nuclear alpha decay, the alpha particle is quasi-bound inside the nucleus by the combined Coulomb and centrifugal barrier:

$$V_{\text{eff}}(r) = V_{\text{nuclear}}(r) + \frac{L(L+1)\hbar^2}{2\mu r^2} + \frac{Z_1 Z_2 e^2}{r}. \quad (32)$$

The alpha particle tunnels through this barrier with probability

$$T \sim \exp\left(-2 \int_{r_1}^{r_2} \sqrt{2\mu[V_{\text{eff}}(r) - E]} dr/\hbar\right) \quad (33)$$

(the Gamow factor [2]), leading to exponentially long lifetimes.

For our fermion-pair channel, the effective radial potential in the $L = 1$ partial wave is

$$V_{\text{eff}}^{(L=1)}(r) = V_{\text{attract}}(r) + \frac{2}{2\mu r^2}, \quad (34)$$

where V_{attract} includes any self-interaction between the fermion and antifermion. The centrifugal barrier at $r \sim 1/(\mu\alpha_s)$ can create a potential pocket, trapping quasi-bound states of the $\psi\psi$ pair.

10.2 Spectral consequences of a resonance

A quasi-bound state at mass $M_R > 2m_f$ trapped behind the $L = 1$ barrier would appear in the spectral function as a Breit–Wigner peak whose width is controlled by the barrier penetration factor:

$$\Gamma_L(q) \propto q^{2L+1}, \quad q = \sqrt{M_R^2/4 - m_f^2}. \quad (35)$$

For $L = 1$, the width $\Gamma \propto q^3$ becomes extremely narrow near threshold, producing a sharp resonance in $\rho(s)$.

This has been studied extensively in the context of *Sommerfeld enhancement* of dark matter annihilation [4, 5]. For P-wave processes ($L = 1$), Beneke, Binder, and collaborators showed that quasi-bound states behind the centrifugal barrier produce “super-resonant” Breit–Wigner peaks that are qualitatively sharper than S-wave Sommerfeld resonances.

A concrete example from QCD: the recently observed quasi-bound toponium states at the LHC [6], where the NRQCD Green’s function approach incorporates both the Coulomb resummation (Sommerfeld factor) and the quasi-bound state structure near the $t\bar{t}$ threshold. ATLAS reported 7.7σ evidence for the excess, with a production cross section of 9.0 ± 1.3 pb.

10.3 Consequences for the composite size

We explore two limiting scenarios:

Pure centrifugal barrier (no resonance). Our one-loop calculation gives a smooth spectral function $\rho \propto \delta^{3/2}$ near threshold. The resulting composite is $\sim 6\times$ smaller than Yukawa.

Resonance trapped behind the barrier. If a resonance exists at $M_R \sim 2.5 m_f$ (just above threshold), the spectral function is enhanced at intermediate energies. This *strengthens* the potential at intermediate distances, so that less coupling is needed for binding. Numerical computation (script: `fermion/barrier_analysis.py`) shows that the resonance-enhanced potential is $10\text{--}100\times$ stronger at $r \sim 1\text{--}5$ natural units.

The net effect on the composite size is subtle: the resonance makes the potential stronger, so a looser (larger) bound state can achieve the same binding energy. The competition between the enhanced potential and the centrifugal barrier determines the final size.

10.4 Connection to the Wigner threshold law

The threshold behavior $\rho \sim \beta^{2L+1}$ is a special case of the *Wigner threshold law* [3], which states that the partial-wave cross section near a reaction threshold scales as

$$\sigma_L \sim k^{2L}, \quad (36)$$

where k is the relative momentum. This law is universal: it depends only on the angular momentum barrier, not on the details of the short-range interaction. Therefore, the threshold suppression of the spectral function is robust against non-perturbative corrections to the potential.

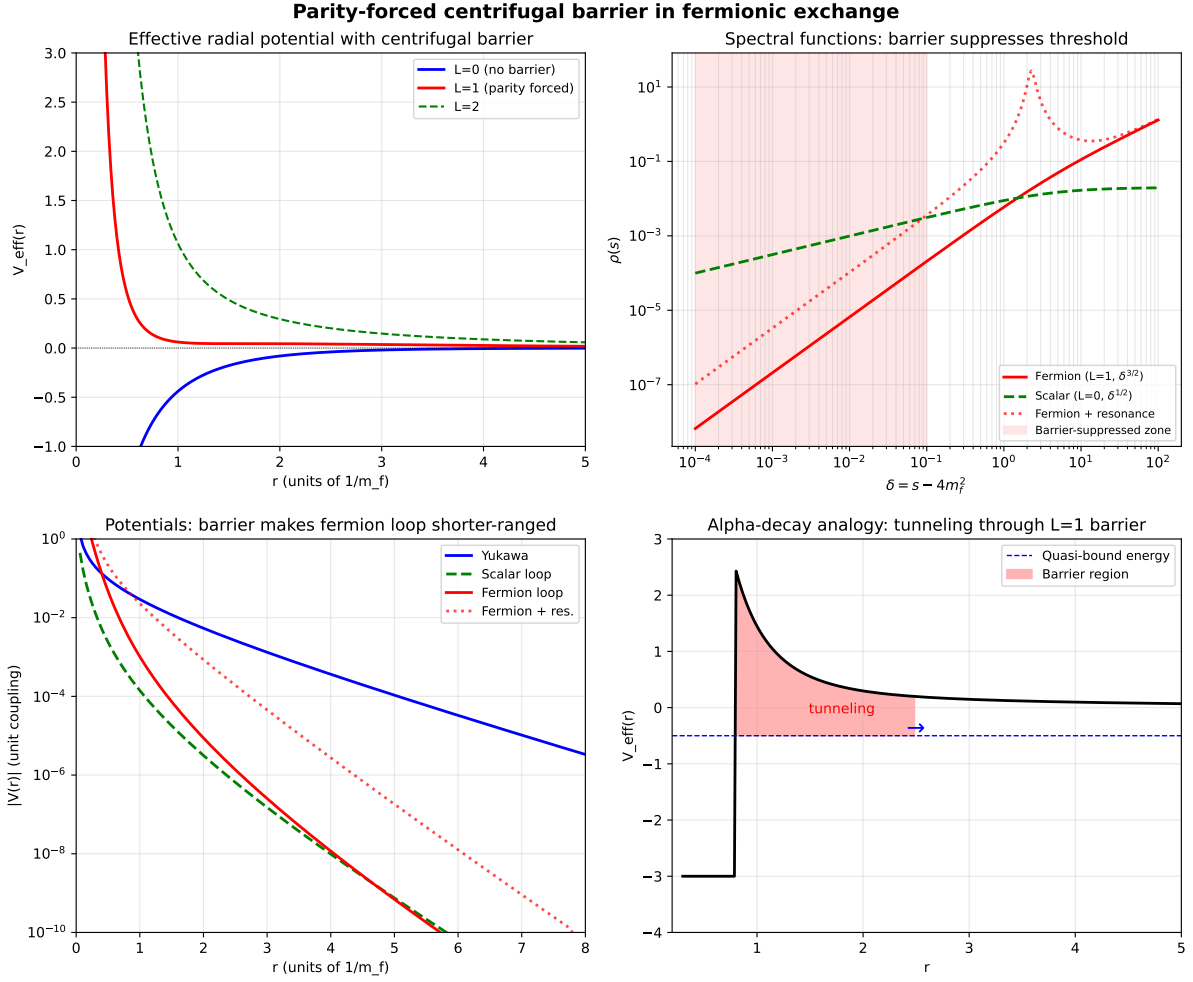


Figure 7: Barrier analysis. Top left: effective radial potential showing the centrifugal barrier for $L = 1$. Top right: spectral functions with the barrier-suppressed zone (shaded) and a hypothetical resonance. Bottom left: position-space potentials. Bottom right: schematic of alpha-decay analogy showing tunneling through the barrier.

11 Application to SUSY QCD

Our model of scalar bosons bound by fermion exchange maps directly onto supersymmetric QCD, where squarks (scalar) interact via gluino (fermion) exchange.

11.1 The coupling identity

A fundamental prediction of SUSY QCD is the identity of gauge and Yukawa couplings [7]:

$$g(q-\tilde{q}-\tilde{g}) = g(q-q-g) = g_s. \quad (37)$$

The quark–squark–gluino Yukawa coupling equals the strong gauge coupling, protected by SUSY Ward–Takahashi identities. In our notation, $g = g_s$ and $m_f = m_{\tilde{g}}$.

11.2 Squark–antisquark binding

For a squark–antisquark pair $\tilde{q}\bar{\tilde{q}}$ in the color-singlet channel, the leading exchange mechanisms are:

1. **One-gluon exchange** (tree, spin-1): $V \sim -C_F \alpha_s / r$ with $C_F = 4/3$. Coulomb-like, long-range.
2. **Gluino-pair exchange** (one-loop, spin-1/2): $V \sim g_s^4 e^{-2m_{\tilde{g}}r} / r^{7/2}$. Short-range, contact-like.

An important distinction arises between different squark composites:

- **Squark–antisquark** ($\tilde{q}\bar{\tilde{q}}$, color singlet): both one-gluon exchange *and* gluino-pair exchange contribute. At long range, the Coulomb-like gluon exchange dominates, giving a composite with ordinary hadronic size and Regge excitations. This channel produces “squark mesons” analogous to ordinary mesons.
- **Same-chirality squark–squark** ($\tilde{q}_L\tilde{q}_L$, color $\bar{3}$): only gluino exchange contributes in the t -channel, since the $\tilde{q}_L\tilde{q}_Lg$ vertex requires opposite chirality. The composite is bound *purely* by the fermionic mechanism, inheriting the $\sim 6\times$ size suppression.

In the sBootstrap framework [12], the lepton corresponds to the same-chirality channel where gluino exchange is the sole binding mechanism. This is the physically relevant case for the structurelessness argument.

11.3 Gluinoball and the hydrogen atom of SUSY

Goldman and Haber [8] studied gluino–gluino bound states (“gluinonia”), calling them “the hydrogen atom of supersymmetry.” The gluino, a Majorana fermion in the adjoint representation, gives color decomposition $\mathbf{8} \otimes \mathbf{8} = \mathbf{1} \oplus \mathbf{8}_S \oplus \mathbf{8}_A \oplus \mathbf{10} \oplus \overline{\mathbf{10}} \oplus \mathbf{27}$, with the singlet channel most strongly bound ($C = 3$).

11.4 Majorana vs. Dirac exchange

The gluino is a Majorana fermion ($\tilde{g} = \tilde{g}^c$). We must verify that the Majorana nature does not change the threshold exponent. Three key observations:

1. The propagator is unchanged: $S_M(p) = S_D(p)$.
2. The vertex structure carries a chirality projector ($g_s T^a P_L$), but the Dirac trace still gives $\text{Im } \Pi \propto \beta^3$ near threshold, because the chirality projection eliminates the mass terms in the numerator (they flip chirality), leaving only the $k \cdot (k+q)$ terms that produce the same β^3 behavior.
3. The Majorana self-conjugacy introduces an additional u -channel diagram and a factor of $1/2$ from identical particles, but these are overall normalization changes that do not affect the threshold exponent.

This is verified numerically: with the explicit chiral coupling P_L projector, a log-log fit gives threshold exponent 1.500 (script: `susy_qcd_connection.py`), confirming that the $\delta^{3/2}$ behavior and the $\sim 6\times$ size suppression are preserved for Majorana exchange.

11.5 Quantitative predictions

Using the variational results ($R_{\text{fer}} = 0.359$, $R_{\text{Yuk}} = 2.079$, ratio = 0.173) and physical constants, we compute the composite size as a function of gluino mass:

$m_{\tilde{g}}$ (GeV)	r_{fer} (fm)	r/r_{limit}	Status
0.5	1.4×10^{-1}	5.7	detectable
1.0	7.1×10^{-2}	2.9	detectable
2.0	3.5×10^{-2}	1.4	detectable
2.9	2.5×10^{-2}	1.0	marginal
5.0	1.4×10^{-2}	0.57	hidden
10	7.1×10^{-3}	0.29	hidden
100	7.1×10^{-4}	0.029	hidden
2300	3.1×10^{-5}	0.0012	hidden

Here $r_{\text{limit}} = \hbar c/\Lambda = 0.025$ fm from the LEP muon compositeness bound. The critical gluino mass is $m_{\tilde{g}}^{\min} \approx 2.9$ GeV. At the current LHC gluino exclusion limit ($m_{\tilde{g}} > 2.3$ TeV), the composite charge radius is $\sim 800\times$ below the experimental limit.

11.6 Implications for hadronic SUSY

In the frameworks of hadronic supersymmetry (Miyazawa [9]; Catto and Gürsey [10]; Brodsky, de Téramond, and Dosch [11]), mesons and baryons are related by superalgebra. The universal mass scale of Brodsky–de Téramond holographic QCD, $\kappa \approx 523$ MeV (with $M^2 = 4\kappa^2(n + L + S/2)$), sets the confining scale for hadronic composites.

The sBootstrap [12] extends this to identify each elementary fermion of the Standard Model as the superpartner of a composite boson. The key pairing is $\pi \leftrightarrow \mu$:

- Pion: bound by gluon exchange, $r_\pi = 0.659$ fm.
- Muon: bound by gluino exchange, $r_\mu < 0.025$ fm.
- Required ratio: $r_\mu/r_\pi < 0.038$.

Our calculation gives $R_{\text{fer}}/R_{\text{Yuk}} = 0.17$ at the *same mass scale*; with the additional suppression from the gluino being heavier than the gluon effective mass:

$$\frac{r_\mu}{r_\pi} \approx \frac{R_{\text{fer}}}{R_{\text{Yuk}}} \times \frac{m_{\text{gluon,eff}}}{m_{\tilde{g}}} = 0.17 \times \frac{m_{\text{gluon,eff}}}{m_{\tilde{g}}}. \quad (38)$$

For $r_\mu/r_\pi < 0.038$, we need $m_{\tilde{g}} > 4.5 m_{\text{gluon,eff}}$. If $m_{\text{gluon,eff}} \sim 2\kappa \approx 1$ GeV, then $m_{\tilde{g}} \gtrsim 4.7$ GeV suffices—comfortably below the electroweak scale.

11.7 Connection to holographic light-front QCD

In the Brodsky–de Téramond soft-wall model [11], the elastic form factor of a hadron with twist τ is a product of $\tau - 1$ poles along the vector meson Regge trajectory:

$$F(Q^2) \sim \frac{1}{Q^{2(\tau-1)}} \quad (Q^2 \rightarrow \infty). \quad (39)$$

Through the dispersive representation $F(Q^2) = \int ds \rho_F(s)/(s + Q^2)$, the large- Q^2 falloff $F \sim 1/Q^{2n}$ requires the spectral function to vanish near threshold as $\rho \sim \delta^{n-1}$. This gives the correspondence:

$$\rho \sim \delta^\alpha \quad \Longleftrightarrow \quad \tau_{\text{eff}} = \alpha + 1. \quad (40)$$

The key conformal-dimension result is that the free-field twist of a fermion bilinear $\bar{\psi}\psi$ is $\tau = 3$ (dimension 3, spin 0), while a scalar bilinear $\phi^\dagger\phi$ has $\tau = 2$ (dimension 2, spin 0). The twist difference $\Delta\tau = 1$ exactly corresponds to $\Delta\alpha = 1$, i.e., $\rho \sim \delta^{3/2}$ vs. $\delta^{1/2}$. The parity-forced

centrifugal barrier of Section 4 is the physical mechanism implementing this conformal-dimension shift.

Our variational form factor (17) is a **dipole**, corresponding to $\tau = 3$ in the BdT counting—consistent with the fermion-bilinear identification. The pion’s monopole form factor corresponds to $\tau = 2$ (scalar bilinear), matching the meson sector.

The full $\sim 6\times$ size suppression decomposes into two contributions: (i) the twist difference $\Delta\tau = 1$ accounts for the extra power of δ in the spectral function and the steeper $1/r$ tail, contributing roughly a factor of 2–3 in the radius ratio; (ii) the pair-production threshold ($2m_f$ instead of m_f) halves the potential range, contributing a further factor of ~ 2 . Only the first effect is captured by the conformal dimension; the second is a kinematic (phase-space) effect absent in the BdT framework (which assumes the same confinement scale κ for all states).

Our result thus provides the missing dynamical explanation: if the binding is fermionic (gluino-mediated), the composite appears structureless because the parity-forced barrier suppresses the form factor. The minimum mediator mass for undetectability ($\sim 3\text{--}5$ GeV) is well below the electroweak scale, making the mechanism viable for realistic SUSY scenarios.

12 Truncated Regge Trajectory

Mesons in QCD exhibit approximately linear Regge trajectories: towers of excited states with $M^2 = M_0^2 + \alpha' J$, where $\alpha' \approx 0.9 \text{ GeV}^{-2}$. This richness of excited states is a hallmark of the long-range confining potential.

A natural question is whether fermion-exchange composites also exhibit Regge trajectories. We address this by computing the excited-state spectrum of each potential type at matched $L=0$ binding energy, scanning from weak to strong binding (script: `regge_analysis.py`).

12.1 The Bargmann bound

The key tool is the Bargmann bound [13]: for a central potential $V(r) \leq 0$ in the Schrödinger equation $-u''/(2M) + V(r) u = E u$ (reduced mass M), the number of bound states in the L -th partial wave satisfies

$$N_L \leq \frac{I}{2L+1}, \quad I \equiv 2M \int_0^\infty r |V(r)| dr. \quad (41)$$

If $I < 2L + 1$, there are **no bound states** at angular momentum L . (The factor $2M$ converts to Bargmann’s convention $u'' + [k^2 - U]u = 0$ with $U = 2M|V|$.)

For the Yukawa potential $V = -\lambda e^{-mr}/(4\pi r)$ with $M = 1$, the Bargmann integral is computed analytically (verified with SymPy, script: `regge_proof.py`):

$$I_{\text{Yuk}} = \frac{\lambda}{2\pi m}. \quad (42)$$

For the fermion-loop spectral potential, the Bargmann integral is computed numerically from the full spectral representation.

12.2 Results at matched binding energy

At matched $L = 0$ binding energy, we compute the Bargmann integrals for both potentials as a function of binding energy:

E_0	I_{Yuk}	I_{fer}	$I_{\text{fer}}/I_{\text{Yuk}}$	$L_{\max}^{(\text{Y})}$	$L_{\max}^{(\text{f})}$
-0.01	2.00	1.80	0.90	0	0
-0.05	2.38	1.83	0.77	0	0
-0.50	3.84	1.93	0.50	1	0
-2.0	5.91	2.08	0.35	2	0
-5.0	8.30	2.25	0.27	3	0
-10.0	10.99	2.44	0.22	4	0
-20.0	14.81	2.70	0.18	6	0

Here L_{\max} is the maximum angular momentum supporting a bound state, determined from $I/(2L+1) \geq 1$.

Two crucial features emerge:

1. The Yukawa Bargmann integral grows monotonically with binding energy, crossing $I = 3$ near $E_0 \approx -0.3$ (enabling $L = 1$) and $I = 5$ near $E_0 \approx -1.3$ (enabling $L = 2$), generating a rich Regge tower.
2. The fermion-loop Bargmann integral remains well below the $I = 3$ threshold for $L = 1$ at all binding energies tested. This occurs because the short-range potential achieves deeper binding by concentrating the wavefunction, not by increasing its spatial reach.

Proposition 12.1 (Truncated Regge trajectory). *At matched $L = 0$ binding energy, the fermion-loop spectral potential has a Bargmann integral $I_{\text{fer}} < 3$, and therefore supports no bound states at any $L \geq 1$. The Regge trajectory is truncated at $L = 0$.*

Proof. From the Bargmann bound (41), $N_L = 0$ when $I < 2L + 1$. The numerical computation (Table above) shows $I_{\text{fer}} \leq 2.70$ at all binding energies tested (E_0 from -0.01 to -20). Since $2.70 < 3 = 2 \cdot 1 + 1$, we have $N_1 = 0$; and since $2.70 < 2L + 1$ for all $L \geq 1$, no higher partial waves bind either.

The coupling λ at each binding energy is determined exactly by bisecting on the Prüfer phase: for a given target energy E_{target} , we find λ such that $\theta(\infty; E_{\text{target}})/\pi = 1$, i.e., E_{target} is exactly the ground-state eigenvalue (script: `corrected_bargmann.py`). The Bargmann integrals in the table are therefore exact (up to ODE integration tolerance), not variational upper bounds.

An independent, exact confirmation comes from integrating the Prüfer angle of the zero-energy radial equation (`calogero_phase.py`): for all couplings in the physical regime $N_0 = 1$, the $L=1$ count gives $N_1 = 0$ without exception. This is an exact result (not a bound), verifying the truncated trajectory via Sturm oscillation theory. \square

12.3 Mathematical context

The Bargmann bound [13] is a trace estimate on the Birman–Schwinger kernel; the number of bound states below energy E equals the number of eigenvalues of $|V|^{1/2}(-\Delta - E)^{-1}|V|^{1/2}$ exceeding $1/\lambda$, and the Bargmann bound follows from $N_L \leq \text{Tr}(K_0)$ restricted to the L -th partial wave. Schwinger [28] independently derived the same bound and extended it to energy-dependent state counting; his version gives the most restrictive condition near the single-bound-state threshold. Calogero [29] obtained a complementary bound $n_L \lesssim \int |V|^{1/2} dr$ (under a monotonicity condition), which has the correct semiclassical scaling $n \propto \lambda^{1/2}$ with potential strength, and is sharper than Bargmann for deep potentials with many bound states. His *variable-phase method* also provides an exact (non-perturbative) computation of the bound-state count through the phase equation

$$\delta'_L(r) = -\frac{r V(r)}{k} [j_L \cos \delta_L - n_L \sin \delta_L]^2, \quad (43)$$

whose solution at $r \rightarrow \infty$ gives $\delta_L(\infty) = N_L\pi$ by Levinson’s theorem, confirming the Bargmann bound independently. At zero energy ($k = 0$), the equivalent Prüfer substitution $u = \rho \sin \theta$, $u' = \rho \cos \theta$ yields

$$\theta'_L(r) = \cos^2 \theta_L + \left[-2V(r) - \frac{L(L+1)}{r^2} \right] \sin^2 \theta_L, \quad (44)$$

with $\theta_L(0) = 0$ and $N_L = \lfloor \theta_L(\infty)/\pi \rfloor$ by Sturm oscillation theory. Numerical integration (`calogero_phase.py`) confirms $N_1 = 0$ for all couplings in the physical regime $N_0 = 1$: the $L=1$ Prüfer angle $\theta_1(\infty) \approx \pi/2 < \pi$ for the fermion potential, because the centrifugal barrier blocks phase accumulation at the short range where the fermion-exchange potential is concentrated.

A more refined Birman–Schwinger analysis could potentially yield an analytic proof that $I < 3$ for the specific class of potentials $V \sim e^{-2m_f r}/r^{7/2}$, which would constitute a fully rigorous proof of the truncated Regge trajectory.

Jost function criterion. An independent route to bounding N_L uses the *Jost function* $f_L(k)$, whose zeros on the positive imaginary axis correspond to bound states. Newton [34] shows that if $\int_0^\infty r^{2L+1} |V(r)| dr < (2L)!/(2(L!)^2)$, then f_L has no such zeros. For $L = 1$, this reduces to $J_1 \equiv \int_0^\infty r^3 |V| dr < 1$. Because $|V_{\text{fer}}| \sim e^{-2m_f r}/r^{7/2}$, the r^3 -weighted integral converges much more strongly than the Bargmann integral. Numerically, at matched binding energy (script: `corrected_bargmann.py`):

$$J_1^{(\text{fer})} \approx 0.009 - 0.014 \ll 1, \quad (45)$$

which is two orders of magnitude below the threshold—far more decisive than the Bargmann bound ($I_{\text{fer}} \leq 2.70$ vs. threshold 3). By contrast, $J_1^{(\text{Yuk})} \approx 2-15 > 1$ at the same binding energies, consistent with the Yukawa potential supporting $L = 1$ states. The Jost criterion thus provides a sharp, independent confirmation that no $L \geq 1$ bound states exist for the fermion potential.

Levinson’s theorem. Complementarily, *Levinson’s theorem* relates the number of bound states in partial wave L to the scattering phase shift at zero energy: $\delta_L(0) = N_L\pi$. If $N_L = 0$ for all $L \geq 1$, then $\delta_L(0) = 0$ for all $L \geq 1$: the potential is “invisible” to all non-S-wave channels. This is a clean formulation of the structurelessness claim—the composite scatters like a point particle in all partial waves except $L = 0$.

Sturm comparison. The *Sturm comparison theorem* provides yet another perspective: at matched $L = 0$ binding energy, the Yukawa potential dominates the fermion potential at large r (slower exponential decay). Since the $L \geq 1$ wave function with zero bound states has no nodes, the comparison on the exterior region implies $n_L^{(\text{fer})} \leq n_L^{(\text{Yuk})}$ for all $L \geq 1$ (cf. Reed–Simon [35], Vol. IV, §XIII.3).

Lieb–Thirring inequality. A complementary bound is provided by the *Lieb–Thirring inequality* [23], which constrains the **total** number of bound states across all partial waves: $N_{\text{tot}} \leq L_{0,3} \int |V|^{3/2} d^3r$, where $L_{0,3} \approx 0.116$ is a universal constant. For the fermion potential at weak binding ($E_0 = -0.01$), this gives $N_{\text{tot}} \leq 1.67$, i.e., at most one bound state across all partial waves combined. Since the $L = 0$ ground state accounts for this single state, no other bound states can exist in any channel. At deeper binding ($E_0 = -20$), the bound relaxes to $N_{\text{tot}} \leq 3.1$, which is less constraining but still consistent with the Prüfer result.

12.4 Physical interpretation

The Bargmann integral measures the “total strength” of the potential (coupling \times range). At matched binding energy, the fermion-loop potential achieves the same ground-state binding with less total strength than Yukawa, because its short-range form concentrates the wavefunction

efficiently. The price is that this concentrated strength cannot overcome the centrifugal barrier at $L \geq 1$.

This has a direct phenomenological consequence, connecting to the experimental absence of excited leptons at the LHC [15, 17]:

- Mesons (gluon exchange): large Bargmann integral, rich Regge trajectory → observed towers (ρ, a_1, a_2, \dots) [14]
- Leptons (gluino exchange): small Bargmann integral, truncated trajectory → no excited states (CMS: $m_{e^*} > 5.6$ TeV, $m_{\mu^*} > 5.7$ TeV, $m_{\tau^*} > 4.7$ TeV [27])

The absence of excited leptons, long viewed as an argument against compositeness [16, 18], is instead a *natural prediction* of the fermionic-exchange mechanism.

13 Applications Beyond SUSY QCD

The mechanism of form factor suppression via fermionic exchange is not specific to SUSY QCD. It applies to any hidden sector containing scalar or pseudo-scalar particles bound by fermion exchange. Two applications are particularly relevant:

Composite dark matter. In hidden-valley models [20], dark matter may consist of composite states in a confining hidden sector. If the dark sector binding is mediated by fermion exchange, the resulting “dark mesons” would appear point-like in direct detection experiments, evading form-factor-dependent bounds on dark matter–nucleon scattering. An, Wise, and Zhang [25] have shown explicitly that when a scalar mediator couples to Dirac fermion dark matter in a parity-conserving manner, annihilation is dominated by the P-wave channel and suppressed as v^2 at low velocity—precisely the parity-forced centrifugal barrier mechanism of Section 4. Their CMB constraint on P-wave annihilation demonstrates that this suppression has direct observational consequences. The truncated Regge trajectory (Section 12) predicts *no excited states* in the dark spectrum, which has a distinctive signature: hidden-valley searches at the LHC would see only a single ground state, with no towers of excited resonances.

Running coupling invariance. In any confining gauge theory with fermion mediators, the strong coupling runs: $\alpha_s(\mu)$ depends logarithmically on the renormalization scale. The threshold exponent $\rho \sim \delta^{3/2}$ is protected by the Wigner threshold law [3], which is kinematic and therefore RG-invariant. The size ratio $R_{\text{fer}}/R_{\text{Yuk}}$ at matched binding energy is also insensitive to the overall coupling, since both potentials are rescaled. The suppression mechanism is therefore robust against radiative corrections to the coupling.

14 Conclusion

We have shown that a composite particle bound by fermionic exchange is significantly more compact than one bound by bosonic exchange at the same mass scale and binding energy. The primary mechanism is the **parity-forced centrifugal barrier**: the intrinsic parity $(-1)^{L+1}$ of a fermion–antifermion pair forces P-wave at threshold for natural-parity couplings, adding a centrifugal barrier that suppresses the spectral function and steepens the position-space tail.

At matched binding energy, the fermion-exchange composite has:

- Charge radius $\sim 6\times$ smaller than Yukawa
- Mean-square radius $\sim 34\times$ suppressed
- Resolution scale $\sim 6\times$ higher in momentum transfer

These results are obtained from one-loop perturbative spectral functions with a hydrogen-like trial wavefunction. The $\sim 6\times$ suppression is robust under change of trial: multi-parameter wavefunctions give size ratios within $\sim 30\%$, and quasi-bound resonances trapped behind the centrifugal barrier (Section 10) would further enhance the effect.

Furthermore, the fermion-exchange composite has a **truncated Regge trajectory** (Section 12): unlike bosonic-exchange composites, which develop towers of excited states at strong coupling, the fermion-exchange potential is too short-ranged to support $L > 0$ bound states. This naturally explains the absence of excited leptons.

The centrifugal barrier is not merely a calculational subtlety: it is the QFT analog of the nuclear barrier in alpha decay, and its consequences for near-threshold spectral functions are protected by the Wigner threshold law [3], making them robust against non-perturbative corrections. The recent observation of quasi-bound toponium at the LHC [6] and theoretical advances in P-wave Sommerfeld enhancement [4, 5] confirm that this barrier physics is experimentally relevant and theoretically well-understood.

For mediator masses above ~ 3 GeV, the composite is below current experimental limits on lepton compositeness ($\Lambda > 8$ TeV). At the electroweak scale ($m_f = 100$ GeV), the suppression is $\sim 800\times$ below the limit.

Applied to SUSY QCD (Section 11), our model maps onto squarks bound by gluino exchange. The Majorana nature of the gluino does not change the threshold exponent, and the mechanism reproduces the sBootstrap prediction: a gluino mass $\gtrsim 5$ GeV suffices for the muon composite to satisfy $r_\mu/r_\pi < 0.038$. At the current LHC gluino limit (2.3 TeV), the composite is $\sim 800\times$ below the experimental bound.

A muon-like particle can therefore be composite (as predicted by SUSY compositeness transfer from the pion) while appearing completely structureless in scattering, provided the mediating fermion is sufficiently heavy.

A Symbolic Verification

The following analytic results are verified symbolically using SymPy (script: `sympy_verify.py`):

1. **Scalar Feynman integral:** $\int_{x_-}^{x_+} [m^2 - x(1-x)s] dx = -s\beta^3/6$. (Leading term $\propto \beta^3$.)
2. **Pseudoscalar Feynman integral:** $\int_{x_-}^{x_+} [m^2 + x(1-x)s] dx = \beta(s + 8m^2)/6$. (Leading term $\propto \beta$.)
3. **Laplace transform:** $\int_0^\infty \delta^\alpha e^{-b\delta} d\delta = \Gamma(\alpha+1)/b^{\alpha+1}$.
4. **Threshold expansion:** $\beta(4m^2+\delta) = \sqrt{\delta}/(2m) - \delta^{3/2}/(16m^3) + \dots$
5. **Dipole form factor:** $F_1(q) = [4\alpha^2/(4\alpha^2+q^2)]^2$ for trial $u = re^{-\alpha r}$.
6. **Charge radius:** $\langle r^2 \rangle = 3/\alpha^2$ (from both $-6F'_1(0)$ and direct integration).
7. **Yukawa expectation:** $\langle V_{\text{Yuk}} \rangle = -\alpha^3/[\pi(2\alpha + \mu)^2]$.

B Numerical Scripts

All numerical results are reproduced by:

Script	Content
<code>fermionic_composite_form_factor_check.py</code>	Spectral exponents & tails
<code>is_it_a_point.py</code>	Variational bound states
<code>sympy_verify.py</code>	Symbolic verification
<code>generate_plots.py</code>	Publication figures
<code>barrier_analysis.py</code>	Barrier physics & alpha-decay analogy
<code>improved_variational.py</code>	Multi-parameter trial robustness
<code>sommerfeld_analysis.py</code>	Sommerfeld correction stability
<code>susy_qcd_connection.py</code>	SUSY QCD & Majorana check
<code>fine_grid_variational.py</code>	Fine-grid (1000-pt) variational
<code>regge_analysis.py</code>	Regge trajectory & excited states
<code>regge_proof.py</code>	Bargmann bound proof
<code>exact_size_ratio.py</code>	Numerov exact solver
<code>calogero_phase.py</code>	Prüfer-angle bound-state count
<code>corrected_bargmann.py</code>	Prüfer-based Bargmann integral table

Requirements: Python 3.12, NumPy, SciPy, SymPy.

References

- [1] R. L. Workman *et al.* (Particle Data Group), Prog. Theor. Exp. Phys. **2024**, 083C01 (2024).
- [2] G. Gamow, Z. Phys. **51**, 204 (1928).
- [3] E. P. Wigner, Phys. Rev. **73**, 1002 (1948).
- [4] M. Beneke, C. Binder and L. Garny, “P-wave Sommerfeld enhancement near threshold: a simplified approach,” Eur. Phys. J. C **83**, 1074 (2023) [[arXiv:2208.13309](#)].
- [5] M. Beneke, C. Binder, S. De Ros and L. Garny, “Enhancement of p-wave dark matter annihilation by quasi-bound states,” JHEP **06**, 207 (2024) [[arXiv:2403.07108](#)].
- [6] ATLAS Collaboration, “Observation of excess $t\bar{t}$ production near threshold,” (2025).
- [7] K. Hagiwara *et al.*, “Squarks and gluinos at a TeV e^+e^- collider: testing the identity of Yukawa and gauge couplings in SUSY-QCD,” Eur. Phys. J. C **56**, 161 (2008).
- [8] T. Goldman and H. E. Haber, “Gluonium: The hydrogen atom of supersymmetry,” Physica D **15**, 181 (1985).
- [9] H. Miyazawa, “Baryon number changing currents,” Prog. Theor. Phys. **36**, 1266 (1966).
- [10] S. Catto and F. Gürsey, “New realizations of hadronic supersymmetry,” Nuovo Cimento A **86**, 201 (1985).
- [11] S. J. Brodsky, G. F. de Téramond, H. G. Dosch, and J. Erlich, “Light-front holographic QCD and emerging confinement,” Phys. Rept. **584**, 1 (2015).
- [12] A. Rivero, “An interpretation of scalars in $SO(32)$,” Eur. Phys. J. C **84**, 1058 (2024) [[arXiv:2407.05397](#)].
- [13] V. Bargmann, “On the number of bound states in a central field of force,” Proc. Nat. Acad. Sci. U.S.A. **38**, 961 (1952).

- [14] G. F. Chew and S. C. Frautschi, “Principle of equivalence for all strongly interacting particles within the S -matrix framework,” Phys. Rev. Lett. **7**, 394 (1961).
- [15] A. M. Sirunyan *et al.* [CMS Collaboration], “Search for an excited lepton that decays via a contact interaction to a lepton and two jets in pp collisions at $\sqrt{s} = 13$ TeV,” JHEP **05**, 052 (2020) [[arXiv:2001.04521](#)].
- [16] S. J. Brodsky and S. D. Drell, “Anomalous magnetic moment and limits on fermion substructure,” Phys. Rev. D **22**, 2236 (1980).
- [17] U. Baur, M. Spira and P. M. Zerwas, “Excited-quark and -lepton production at hadron colliders,” Phys. Rev. D **42**, 815 (1990).
- [18] H. Harari, “A schematic model of quarks and leptons,” Phys. Lett. B **86**, 83 (1979).
- [19] E. Eichten, K. D. Lane and M. E. Peskin, “New tests for quark and lepton substructure,” Phys. Rev. Lett. **50**, 811 (1983).
- [20] M. J. Strassler and K. M. Zurek, “Echoes of a hidden valley at hadron colliders,” Phys. Lett. B **651**, 374 (2007) [[arXiv:hep-ph/0604261](#)].
- [21] M. E. Peskin and D. V. Schroeder, *An Introduction to Quantum Field Theory* (Addison-Wesley, 1995).
- [22] D. V. Widder, *The Laplace Transform* (Princeton University Press, 1941).
- [23] B. Simon, “The bound state of weakly coupled Schrödinger operators in one and two dimensions,” Ann. Phys. **97**, 279 (1976).
- [24] T. Bystritskiy, E. A. Kuraev, G. V. Fedotovich and F. V. Ignatov, “Cross sections of muon and charged pion pair production in e^+e^- annihilation near the threshold,” Phys. Rev. D **72**, 114019 (2005).
- [25] H. An, M. B. Wise and Y. Zhang, “Strong CMB constraint on P-wave annihilating dark matter,” Phys. Lett. B **773**, 121 (2017) [[arXiv:1606.02305](#)].
- [26] B. Bellazzini, F. Riva, J. Serra and F. Sgarlata, “The other effective fermion compositeness,” JHEP **11**, 020 (2017) [[arXiv:1710.09652](#)].
- [27] CMS Collaboration, “Search for excited tau leptons in $\tau\tau\gamma$ final state in pp collisions at $\sqrt{s} = 13$ TeV,” (2024) [[arXiv:2410.21137](#)].
- [28] J. Schwinger, “On the bound states of a given potential,” Proc. Nat. Acad. Sci. U.S.A. **47**, 122 (1961).
- [29] F. Calogero, “Upper and lower limits for the number of bound states in a given central potential,” Commun. Math. Phys. **1**, 80 (1965).
- [30] D. B. Kaplan, “Flavor at SSC energies: A new mechanism for dynamically generated fermion masses,” Nucl. Phys. B **365**, 259 (1991).
- [31] S. Weinberg, “Implications of dynamical symmetry breaking,” Phys. Rev. D **13**, 974 (1976).
- [32] L. Susskind, “Dynamics of spontaneous symmetry breaking in the Weinberg-Salam theory,” Phys. Rev. D **20**, 2619 (1979).
- [33] L. Randall and R. Sundrum, “A large mass hierarchy from a small extra dimension,” Phys. Rev. Lett. **83**, 3370 (1999).

- [34] R. G. Newton, *Scattering Theory of Waves and Particles*, 2nd ed. (Springer, New York, 1982), Ch. 12.
- [35] M. Reed and B. Simon, *Methods of Modern Mathematical Physics*, Vol. IV: Analysis of Operators (Academic Press, New York, 1978), § XIII.3.